

Review

Preparation and Applications of Rare-Earth-Doped Ferroelectric Oxides

Taiyu Bian, Tianhong Zhou and Yang Zhang *

Institute of Modern Optics & Tianjin Key Laboratory of Micro-Scale Optical Information Science and Technology, Nankai University, Tianjin 300071, China

* Correspondence: yangzhang@nankai.edu.cn

Abstract: Ferroelectric oxides possess abundant fascinating physical functionalities, such as electro-optic, acousto-optic, and nonlinear optical characteristics, etc. However, most pristine ferroelectric oxides exhibit no efficient luminescent properties due to the indirect and wide bandgap. Rare-earth-doped phosphors demonstrate advantages such as sharp emission bandwidths, large Stokes shift, high photon stability, and low toxicity. The combination of rare-earth ions and ferroelectric oxides has shown great potential in optical sensing, lighting, solar cells, and other applications. Rare-earth-doped ferroelectric oxides exhibit efficient upconversion or downconversion luminescence in the range of ultraviolet (UV) to near-infrared (NIR) regions. In this article, the preparation process of rare-earth-doped ferroelectric oxides and the preparation methods of thin films are introduced. Their recent applications in optical sensing, lighting, and solar cells are highlighted. The review concludes with a brief summary of all related branches and discusses the potential direction of this field.

Keywords: rare earth; upconversion luminescence; ferroelectrics; thin films



Citation: Bian, T.; Zhou, T.; Zhang, Y. Preparation and Applications of Rare-Earth-Doped Ferroelectric Oxides. *Energies* **2022**, *15*, 8442. <https://doi.org/10.3390/en15228442>

Academic Editor: Prodip K. Das

Received: 30 September 2022

Accepted: 10 November 2022

Published: 11 November 2022

Publisher's Note: MDPI stays neutral with regard to jurisdictional claims in published maps and institutional affiliations.



Copyright: © 2022 by the authors. Licensee MDPI, Basel, Switzerland. This article is an open access article distributed under the terms and conditions of the Creative Commons Attribution (CC BY) license (<https://creativecommons.org/licenses/by/4.0/>).

1. Introduction

Rare-earth elements have unique structural characteristics and physical and chemical properties. After long-term research and accumulation of rare-earth ions, rare-earth-doped materials are widely used in photonic devices, flat panel displays, optical sensors, and other multifunctional optical devices. Rare-earth elements comprise Scandium (Sc), Yttrium (Y), and 15 lanthanides. The lanthanides include Lanthanum (La), Cerium (Ce), Praseodymium (Pr), Neodymium (Nd), Promethium (Pm), Samarium (Sm), Europium (Eu), Gadolinium (Gd), Terbium (Tb), Dysprosium (Dy), Holmium (Ho), Erbium (Er), Thulium (Tm), Ytterbium (Yb), and Lutetium (Lu). Lanthanide atoms have shell configurations of $1s^2 2s^2 2p^6 3s^2 3p^6 3d^{10} 4s^2 4p^6 4d^{10} 4f^{0-14} 5s^2 5p^6 5d^{0-1} 6s^2$. Rare-earth ions possess unique energy level structures and have attracted extensive research attention around the world. They are often doped in thin films, ceramics, single crystals, and other materials, which are used in lighting devices, displays, sensors, and other multifunctional devices [1,2]. Among them, rare-earth ions, as luminous centers (also known as activators), generate different radiative transitions under irradiation. When the activator shows a weak absorption cross-section, other kinds of impurity ions will be co-doped in the matrix material. Such other kinds of impurity ions are called sensitizers [3]. The sensitizer ion-absorbing photon transitions to the excited state, and during the process of returning to the ground state, the sensitizer ion will transfer energy to the activator ion, as shown in Figure 1. The doped lanthanide ions are often referred to as Ln^{3+} . The 5d–4f level transition allowed by parity (such as Ce^{3+}) and the 4f–4f level transition prohibited by parity occur in Ln^{3+} ions. Lanthanide ions characterized by partially filled 4f shells are shielded from the surrounding environment by filled 5s² and 5p⁶ orbitals, resulting in sharp and narrow emission lines of transitions within 4f structures. However, because 5d electrons are not shielded, the emission spectrum generated by the 5d–4f transition (such as Ce^{3+}) generally has a

broad band. Therefore, the surrounding environment of different energy levels has a great influence on the emission spectra generated by energy level transitions.

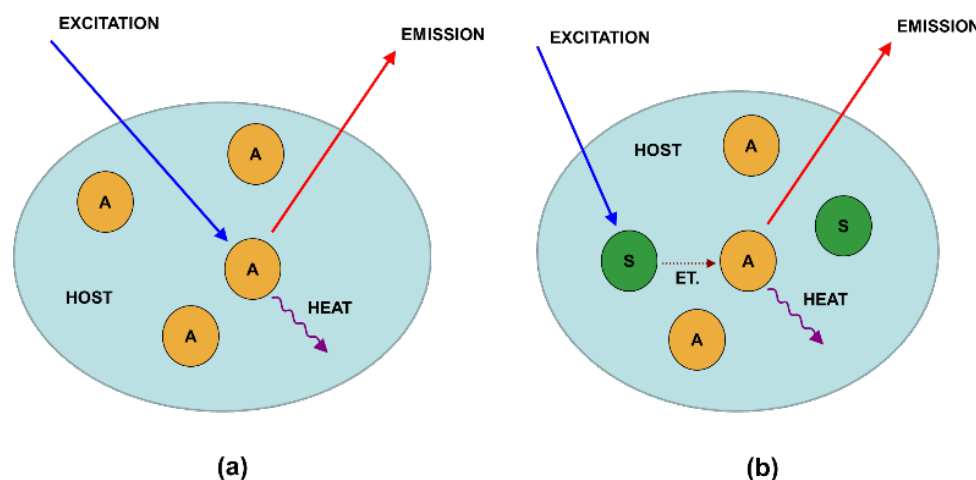


Figure 1. (a) Only activators participate in the luminescence process. (A is the activator and S is the sensitizer.) (b) The luminescence process has the simultaneous action of activator and sensitizer. Reprinted with permission from [1] © 2013 Royal Society of Chemistry.

For the lifetime of emission photons, the lifetime of emission photons generated by 4f-4f transition is longer than that generated by 5d-4f transition. Due to the forbidden characteristic of f-f transition in 4f ions, the lifetime of emitted photons generated by 4f-4f transition is milliseconds [4]. At present, some Ln³⁺ ions (Er³⁺, Tm³⁺, Ho³⁺ and Pr³⁺) with rich energy levels have been widely studied as activators of luminescent materials. Rare earth ion-doped ferroelectric oxides exhibit excellent upconversion or downconversion luminescence in the ultraviolet (UV) and near-infrared (NIR) regions [5–7]. The 4f energy level diagram of some rare-earth ions is shown in Figure 2 [8]. Upconversion and downconversion luminescence are both photoluminescence processes. This process is a luminescence phenomenon caused by the radiation transition of electrons from the ground state to the excited state under excitation. For upconversion luminescence, when the ground-state electron absorbs a photon, it transits from the ground state to a higher-level excited state, and then the excited-state electron transits to a relatively lower excited state through the nonradiative transition. Then, the electron in the excited state absorbs another photon, which transits to a higher excited state. Then, the photon through radiation transits back to the ground state, releasing a short-wavelength photon. For downconversion luminescence, when the ground-state electron absorbs the energy of a short-wavelength (high energy) photon, it transits from the ground state to a higher energy level excited state. Then, the excited-state electron transits to a relatively lower excited state through nonradiation. The lower excited state transits back to the ground state through radiative transition, which releases a long-wavelength photon at the same time.

Perovskite oxide ferroelectrics possess abundant fascinating physical functionalities. BaTiO₃ (BTO) and LiNbO₃ demonstrate superior electro-optic, acousto-optic, and nonlinear optical characteristics, which are very beneficial for photonic applications [9]. Ferroelectric oxides exhibit spontaneous polarization under the Curie temperature. This spontaneous polarization will change repeatedly upon the external electric field. Pristine ferroelectric oxides cannot emit efficient luminescence because of the indirect and wide bandgap nature. Perovskite oxides such as SrTiO₃(STO) can emit blue photoluminescence (PL) from band-to-band radiative recombination only under low temperature. Rare-earth ions have abundant energy levels, sharp emission bandwidths, and large Stokes shift, which are regarded as important for phosphor choices [10]. So, rare-earth-doped ferroelectric oxides are endowed with efficient luminescent properties [11]. Some high-functional ferroelectric oxides have solid crystal fields and low vibration frequencies. These Ln³⁺ ions provide a suitable

matrix material. Ferroelectricity, piezoelectricity, and photoexcitation based on Ln^{3+} -doped ferroelectrics have many applications in various aspects [12].

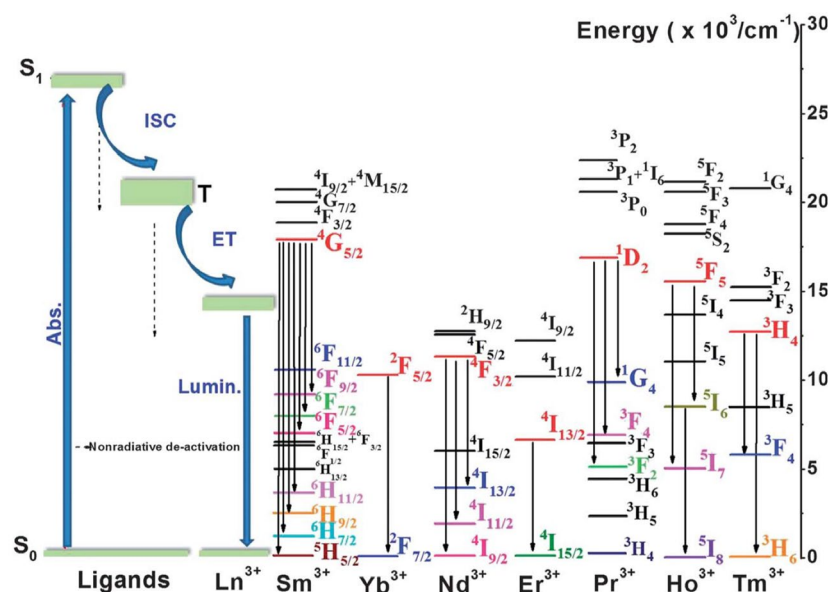


Figure 2. Photosensitization process and 4f energy level diagrams of some rare-earth ions. Reprinted with permission from [8] © 2013 Royal Society of Chemistry. (Abs is absorbing. ISC is intersystem crossing. T is the triplet state. ET is the energy transfer).

In the rare-earth-doped ferroelectric oxide luminescence, some of the rare-earth ions as the luminescence center have rich trapezoidal energy levels. The ferroelectric oxide matrix provides a suitable crystal field and environmental energy for the luminescence center. The rare-earth-doped ferroelectric oxides exhibit upconversion or downconversion luminescence. In recent years, the luminous efficiency and control means of doped ferroelectric materials have been extensively studied. Meanwhile, the performance of upconversion and downconversion luminescence has been further developed [13–15]. Many applications of rare-earth-doped ferroelectric oxides, such as sensing, lighting, and solar cells, are emerging. In this article, we summarize the preparation methods of rare-earth-doped ferroelectric oxide and discuss the synthesis and structural influence on their luminescent properties. In the last part of the article, we highlight the progress in the applications of rare-earth-doped ferroelectric oxides.

2. Ferroelectric Oxides

Ferroelectric oxides can be insulators, metals, and even topological ferroelectric metals [16]. Herein, this article focuses on the luminescent properties and photonic applications of rare-earth-doped ferroelectric insulator oxides. The ferroelectric material has spontaneous polarization (P) that can be switched by the applied electric field (E), and the destruction of the symmetry of the spatial inversion allows the charge center unit separation, which is a prerequisite for the emergence of ferroelectric polarization [17]. The remaining magnetization is distributed among the oxygen ligands due to the itinerant spin-polarized electrons [18].

2.1. Crystal Field for The Luminescence Center

For rare-earth-doped ferroelectric oxides, we take the bismuth layer structure ferroelectrics (BLSFs) family as an example. BLSFs are expressed as $\text{Bi}_2\text{A}_{m-1}\text{B}_m\text{O}_{3m+3} = (\text{Bi}_2\text{O}_2)^{2+}(\text{A}_{m-1}\text{B}_m\text{O}_{3m+3})^{2-}$, where A is a large 12-coordinate cation, B is a small 6-coordinate cation, and the electronic configuration is d^0 . A can be monovalent, divalent, trivalent ions, or their mixtures; B represents tetravalent, pentavalent, or hexavalent ions; the subscript m and m-1 subtables are the number of sample octahedron and pseudoperovskite units.

Peng et al. studied Er doping into $\text{CaBi}_4\text{Ti}_4\text{O}_{15}$ [5]. For $\text{CaBi}_4\text{Ti}_4\text{O}_{15}$, $1/2\text{Bi}^{3+}$ ions are located in the $(\text{Bi}_2\text{O}_2)^{2+}$ layer, $1/2\text{Bi}^{3+}$ ions and all Ca^{2+} ions are dispersed at site A, and Ti^{4+} ions occupy site B. Er^{3+} ions can enter the A position of the pseudoperovskite block, randomly replacing Bi^{3+} or Ca^{2+} ions. The radius of Er^{3+} (0.88 Å) ions is much smaller than that of Bi^{3+} (1.03 Å) and Ca^{2+} (1.07 Å) ions. According to the Judd–Ofelt (J-O) theory, PL emission is affected by the local crystal field around rare-earth ions, thus affecting the structural symmetry of the host body [19]. High structural symmetry will lead to weak PL emission. Lanthanide ion doping will preferentially replace the A position in the lattice and occupy the position with anti-center three-position symmetry. Because the radius of doped ions is smaller than that of the original position, the symmetry will be reduced. In principle, when the rare-earth ions are located in the low symmetry position, the electric dipole transition probability of doped rare-earth ions increases. In other words, the low symmetry host body usually imposes a crystal-field high-symmetry counterpart containing more heterogeneous components around the doped ions [20]. The inhomogeneous component enhances the electronic coupling between the 4f level and higher 4f5d configuration, and then increases the f-f transition probability of doped ions. Therefore, when the laser pump power is low, the corresponding light emission also has high intensity. In addition, compared with pure ferroelectric materials, the dielectric loss of ferroelectric materials doped with rare-earth ions increases with temperature, and the loss value after doping is lower than that of pure ferroelectric materials. In the hysteresis loop of Pr ions doped with $(\text{Ba}_{0.99}\text{Ca}_{0.01})(\text{Ti}_{0.98}\text{Zr}_{0.02})\text{O}_3(\text{BCZT})$ reported by Wang, it was found that Pr ions' doping will affect the polarization and coercive field of BCZT ceramics [21]. The doped ferroelectric materials will obtain enhanced remanent polarization.

2.2. Physical Properties of The Rare-Earth-Doped Ferroelectrics

Ferroelectrics have P-E hysteresis loops, which are caused by domain polarization conversion and domain wall movement. The hysteresis loop will contain information such as maximum polarization, residual polarization, and coercive field (E_C), which also reflects the characteristics of ferroelectrics. The loop area of the hysteresis loop represents the energy consumed in the process of polarization switching.

In Yao's research on $\text{BiFeO}_3(\text{BFO})$, the Fe^{3+} and Bi^{3+} ions are shifted along the pseudocubic (111) direction from the center of the oxygen octahedron and the ideal position between the two octahedrons, respectively [22]. These shifts contribute to the enhancement in the spontaneous polarization of rare-earth-doped BFO. Indeed, the shifts in Bi^{3+} were shown to have a stronger influence on the ferroelectric properties of BFO. Secondly, counterrotations of the oxygen octahedra around the pseudocubic (111) axis will lead to rhombohedral symmetry (space group rare-earth ions) with a unit cell doubling compared with the perovskite primitive unit cell. Raman spectra indicated that the rare-earth ions' dopant occupied the Bi-sites in the BFO unit cell. Consequently, the rare-earth ions' dopant might also affect the shift of Bi^{3+} ions along the polar (111) axis, and this dominantly determines the ferroelectric properties of BFO. Therefore, the ferroelectric behaviors of rare earth ions-doped BFO are modified.

Compared with pure BCZT ceramics, the Curie temperature (T_C) of Pr-ion-doped BCZT ceramics increased slightly. The T_C (118 °C) of $(\text{Pr}_{0.002}\text{Ba}_{0.988}\text{Ca}_{0.01})(\text{Ti}_{0.98}\text{Zr}_{0.02})\text{O}_3(\text{BCZT-A})$ ceramics is negligibly affected by doping with Pr ions, while the T_{O-T} expands and shifts to lower temperature. The doping of Pr ions influences the polarization as well as the coercive field of the BCZT ceramics. When Pr ions are doped in BCZT ceramics, $\text{Pr}^{3+}/\text{Pr}^{4+}$ ions occupy the $\text{Ba}^{2+}/\text{Ca}^{2+}$ sites in the BCZT lattice and act as donors, thus enhanced remanent polarization is obtained.

2.3. Influence of Domain Wall and Oxygen Vacancies

In order to reduce the electrostatic energy, ferroelectrics tend to split into domains separated by domain walls and are polarized in different directions. In ferroelectric thin films, defects such as oxygen vacancies near the domain walls lead to domain wall pinning,

which decreases the mobility of the domain walls and ultimately reduces the residual polarization value and increases leakage current density [23]. Furthermore, A-site vacancies will benefit the domain wall motion, which will lead to the low coercive field and slanted P–E loops. Therefore, the enhancement of residual polarization values can be attributed to the increased domain wall mobility through doping.

The existence of oxygen vacancies also affects the ferroelectric properties. Rare-earth-doping bismuth ferrites reported by Verma showed that doping a small amount of Sm^{3+} at the Bi^{3+} site would stabilize the perovskite structure of BFO, thereby reducing the number of oxygen vacancies and subsequently increasing the dielectric constant [24]. The decrement in dielectric constant is related with the hopping of the electrons from Fe^{2+} to Fe^{3+} ions. At low frequency, the electric field does not provide enough energy to the electron for hopping, but as we increase the frequency of electric field, it then provides sufficient energy and a point is reached when hopping of the electron is started from Fe^{2+} to Fe^{3+} ions. Therefore, the conductivity of the dielectric increases as frequency is increased. Hence, a decrement occurs in ϵ' . The dielectric constant of doped BFO is larger than that of undoped BFO. This dielectric behavior of doped BFO might be connected in terms of oxygen vacancy and displacement of Fe^{3+} ions. There are always some oxygen vacancies in undoped BFO, which result in relatively high conductivity and a lower dielectric constant. The doping of rare-earth ions on the A site reduces the generation of oxygen vacancies [22,24]. Meanwhile, fewer oxygen vacancies lead to low leakage current density. Due to the reduction in the leakage current component, better P–E loops can be obtained. The squareness of the P–E loops is increased by adding rare-earth dopants.

In addition, the improved piezoelectric properties and luminescence properties are due to the particular structure of BCZT-A ceramics: the coexistence of the O-T phase at room temperature, the asymmetric local environment, and the homogeneous microstructure. The asymmetric structure, coexistence of orthorhombic and tetragonal phases at room temperature, and fewer oxygen vacancies may be the reasons for the excellent luminescence properties of the BCZT-A ceramics [21].

3. Preparation of Rare-Earth-Doped Ferroelectric Oxides

The preparation methods of rare-earth-doped ferroelectric oxides mainly include solid-phase sintering, liquid-phase synthesis, spray and freeze drying, spray thermal decomposition, microwave-assisted synthesis, combustion synthesis, and physical vapor deposition. Solid-phase reaction and liquid-phase synthesis are the main and most used methods for preparing rare-earth-doped ferroelectric oxides.

3.1. Solid-State Reaction Method

The solid-state reaction method is one of the most used preparation methods for perovskite oxide materials. The solid-phase reaction method usually goes through weighing, ball milling, presintering, grinding, target pressing, and target sintering steps. The temperature of synthesis with this method is usually between 1000 and 1500 °C, and the synthesis time takes about 8 to 24 h. In the process of solid-phase sintering, cations migrate and move through the grain, and finally form the material with perovskite structure. The calcination time, solubility of cations in solid and liquid, and sintering temperature will affect the final product. The sintering temperature is the most important factor on the crystal structure of the product. As for the calcination time, Waandich et al. found that rare-earth-doped ferroelectric materials BaCO_3 , CoCO_3 , and Fe_2O_3 were calcined at 1250 °C for different times, and many small holes appeared inside the materials [25]. For the solubility of cations in the solids, because of the low solubility of some cations in the solids, the final compounds appear in two kinds of phases upon the XRD characterization [26]. For the $\text{BaCo}_{0.7}\text{Fe}_{0.2}\text{Ti}_{0.1}\text{O}_{3-\delta}$ perovskite material, the material completely reacts when the temperature is above 900 °C, and there are many incomplete reactions in the material when the temperature is less than 900 °C.

3.2. Liquid-Phase Synthesis

Liquid-phase synthesis methods include the sol-gel method [27,28], precipitation method [29], hydrothermal method [30,31], and so on. As shown in Figure 3a, the sol-gel method is through hydrolysis or polymerization of the salt compound's reaction, preparation of the metal oxide or metal hydroxide uniform sol, after drying and the heat treatment process to obtain the final products [32]. The purity of nanoparticles prepared by the sol-gel method is higher, and the synthesized particles have good homogeneity and dispersion. Lotey et al. synthesized undoped and Gd-doped BiFeO_3 nanoparticles by the sol-gel method, which were successfully applied for preparing the dye-sensitized solar cells (DSSC) [33].

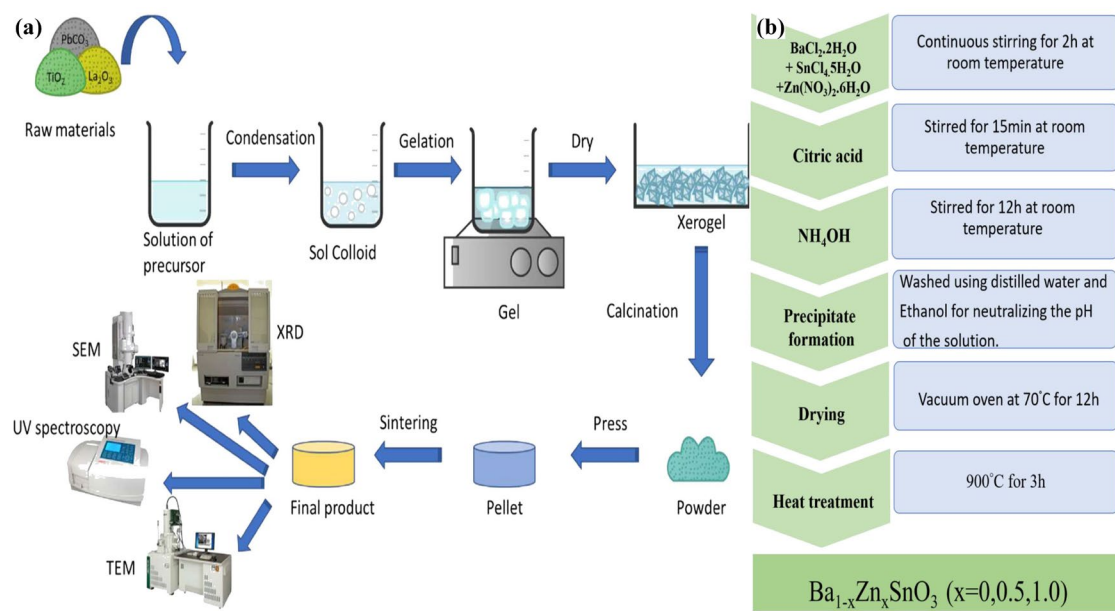


Figure 3. (a) Sol-gel method. Reprinted with permission from [32] © 2020 Elsevier Ltd. (b) Zn-doped BSO by co-precipitation method. Reprinted with permission from [34] © 2021 Elsevier Ltd.

The precipitation method includes the direct precipitation method and co-precipitation method. The direct precipitation method is to add the precipitant into the metal salt solution, and then the precipitate will be obtained after the reaction. The precipitate will be separated from the solution, and then the nano-oxide material can be obtained by decomposing the precipitate. The advantage of the direct precipitation method is that the operation process is simple. However, the particle size prepared by this method is not uniform, and the size is not easy to control. In the co-precipitation method (Figure 3b), the precipitator is added to the mixed salt solution, and then the evenly mixed precipitate is obtained. The final nanomaterials are obtained by heating the precipitate for it to decompose. The co-precipitation method is suitable for the preparation of materials with small particle size and various metallic elements. For example, Reshma Dileep K prepared Zn-doped BaSnO_3 (BSO) by the co-precipitation method and applied it for photovoltaic devices [34].

The hydrothermal method is a method of preparing materials in a high-pressure reaction kettle under high temperature and pressure and using water as the reaction medium (Figure 4). The advantages of the hydrothermal method lie in the good crystallinity and shape control of the powder. For example, Wang synthesized CuBi_2O_4 by the hydrothermal method and analyzed the morphology of CuBi_2O_4 at different hydrothermal times by SEM. They analyzed the UV-vis diffuse reflectance spectrum of CuBi_2O_4 at different hydrothermal times [35].

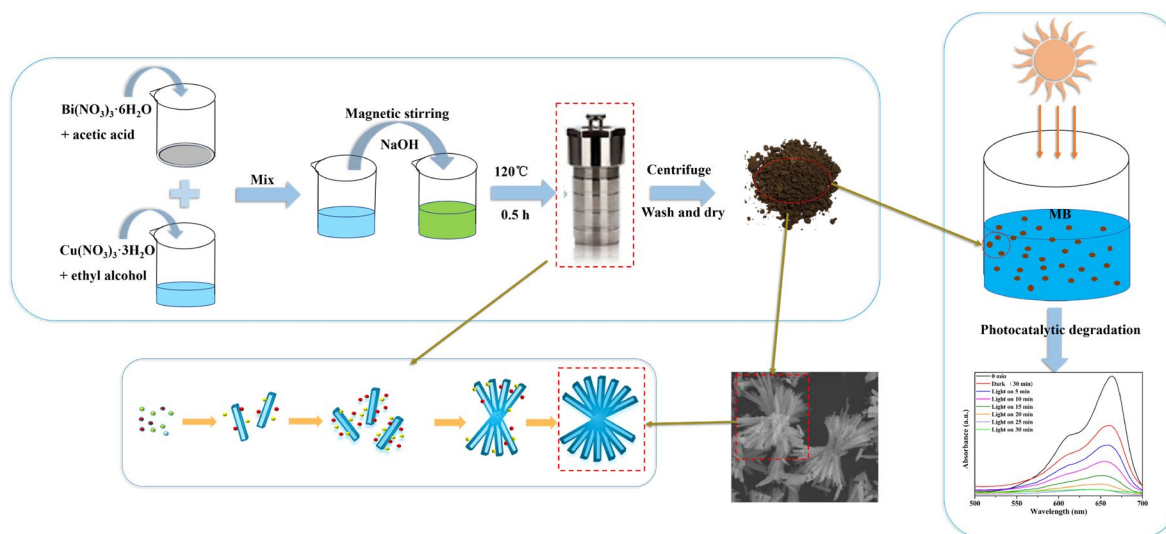


Figure 4. Preparation of CuBi₂O₄ by hydrothermal method, morphology of CuBi₂O₄ under different hydrothermal time, and UV-vis diffuse reflectance spectrum of CuBi₂O₄ under different hydrothermal times. Reprinted with permission from [35] © 2020 MDPI.

3.3. Other Methods

There are also some other methods for the preparation of ferroelectric oxide materials, which are mainly for the synthesis of nanomaterials. These methods include spray and freeze drying, spray pyrolysis, microwave-assisted synthetic sintering, combustion synthesis, and physical vapor deposition. For the spray drying method, mixed raw materials are atomized into small droplets, which are then dried at high temperature to obtain the desired materials. Freeze-drying, also known as sublimation drying, freezes raw materials in a liquid solvent into a solid state at a lower temperature. Under vacuum, frozen solid material sublimates directly into a gas phase and removes water. During freeze-drying, the dilution salts are separated to a minimum and the ions are tightly mixed. The advantages of spray- and freeze-drying are that the ceramic particles synthesized have uniform size, which can effectively control the morphology and composition of the products. Guo et al. reported that the complete anatase phase with large surface area could be obtained by freeze-drying compared with supercritical fluid extraction or oven drying [36]. Klvana reported that La_{0.66}Sr_{0.34}Ni_{0.3}Co_{0.7}O₃ (LSNC) and La_{0.6}Sr_{0.4}Fe_{0.4}Co_{0.6}O₃ (LSFC) perovskite oxide materials were prepared by the freeze-drying method [37]. The spray pyrolysis method involves spraying the metal salt solution in a high temperature environment, which results in the volatilization of the solvent in the metal salt solution, the thermal decomposition of the metal salt, and the saturation precipitation of the ferroelectric oxide nanomaterials in the solvent. Rashidi et al. reported the synthesis of zinc oxide (ZnO) nanoparticles by the spray pyrolysis method [38]. The microwave sintering method is based on microwave and material reaction temperature to achieve high temperature sintering. The advantage of this method is that a material with good density can be prepared, and the pure-phase ceramic material can be obtained at low temperatures. Zhang reported that LiNi_{0.5}Mn_{1.5}O₄ was synthesized by the microwave solid-phase method [39]. The micrograph showed that the particle size was smaller and more compact than that of the traditional calcination method. The combustion synthesis method uses the autoreactive heat release of raw materials to promote the spontaneous synthesis of raw materials.

4. Rare-Earth-Doped Ferroelectric Oxide Thin Films

Rare-earth-doped ferroelectric oxide thin films are of significance for both scientific and technological aspects. Luminescent thin films have been developed for various luminescent devices, such as displays and light sources, solar cells, and sensors. Both physical vapor deposition (PVD) and chemical methods have been used to fabricate rare-earth-doped

ferroelectric thin films. The main difference between PVD and chemical methods is whether chemical reactions occur in the preparation process. In PVD, the pure source material is vaporized in a vacuum by evaporation, laser etching, or sputtering. No chemical reaction occurs in this process. In chemical methods, the source material is mixed with a volatile precursor as a carrier. The mixture is then transported to the reaction chamber over or in contact with the heated substrate. When the mixture is adsorbed on the surface of the substrate, they undergo a chemical reaction to leave a desired source material layer on the substrate. The gas by-products produced by the reaction are discharged through the exhaust port of the chamber. The process of this reaction can be accelerated by heating or plasma.

4.1. Pulsed Laser Deposition

Pulse laser deposition (PLD) [40] is a common PVD method for depositing thin films, which can be traced to the ruby laser deposition by Breech and Cross [41]. Figure 5a shows the PLD system. With the development and exploration of pulsed laser deposition and the rapid development of laser technology, PLD has many advantages, such as high deposition rate, low substrate temperature requirements, and uniform thin films [42,43]. In PLD, a focused pulsed laser impinges on a target (material to be deposited). The laser pulse evaporates or ablates the target material. Then, the ablated material is ejected in the form of a plasma plume and is deposited on the substrate to form a thin film. The quality of PLD thin films is seriously affected by the growth conditions, such as background gas pressure, laser energy density, laser repetition rate, growth temperature, and target substrate separation. For example, Chen deposited Er^{3+} -doped $\text{Na}_{0.5}\text{Bi}_{2.5}\text{Nb}_2\text{O}_9$ (NBN) thin films on polyimide (PI) substrates using PLD deposition technology [44]. Figure 6i is an XRD and TEM diagram of the deposited thin film. Based on this structure, they developed a flexible optical memory. In addition, Wu deposited $\text{Yb}^{3+}/\text{Er}^{3+}$ co-doped BaTiO_3 (BTO: Yb/Er) thin films on piezoelectric $\text{Pb}(\text{Mg}_{1/3}\text{Nb}_{2/3})_{0.7}\text{Ti}_{0.3}\text{O}_3$ (PMN-PT) substrates using PLD deposition technology, which proved the strain engineering tuning of upconversion PI of BTO: Yb/Er thin films grown on PMN-PT substrates [45]. The PL intensity can be modulated in situ and reversibly by the applied electric field. The device structure and thin film characterization analysis of Wu are shown in Figure 6ii.

4.2. Sputtering

Sputtering is another PVD deposition method. Sputtering is to inject an appropriate amount of gas (generally argon Ar) into the reaction chamber under a vacuum environment. Under an appropriate pressure, the free electrons in the reaction chamber will collide with Ar molecules, and Ar will dissociate to generate an Ar ion stream to impact the target, which will precipitate and accumulate the material atoms or molecules of the target on the substrate to form a thin film. This method can deposit thin compound films with controllable stoichiometry and composition at a high deposition rate and industrial scale [47].

4.3. Molecular Beam Epitaxy

Molecular beam epitaxy (MBE) is a technique for growing high-quality thin films on substrates. Under vacuum conditions, steam is generated by heating in a furnace equipped with various required components, collimated through small holes to form molecular beams, and then directly sprayed onto the substrate at the same temperature to form a thin film. For example, Song in 2020 prepared a La-doped $\text{Hf}_{0.5}\text{Zr}_{0.5}\text{O}_2$ thin film by molecular beam epitaxy. Figure 5b is the XRD of the thin film they prepared [46].

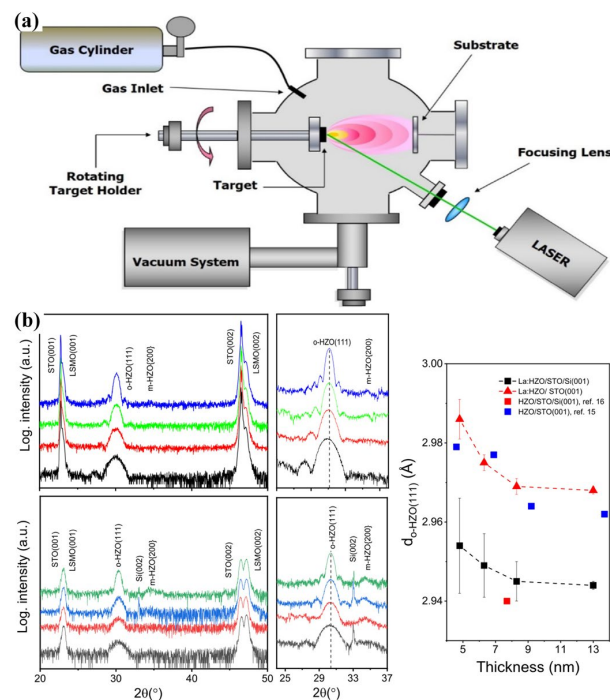


Figure 5. (a) The system of pulsed laser deposition. Reprinted with permission from [40] © 2020 MDPI. (b) XRD θ - 2θ scans of La: HZO thin films on LSMO/STO (001) and LSMO/STO/Si (001), the out of plane o-HZO (111) lattice distance of La: HZO thin films on LSMO/STO (001) (red triangle) and LSMO/STO/Si (001), plotted as a function of thickness. Reprinted with permission from [46] © 2020 American Chemical Society.

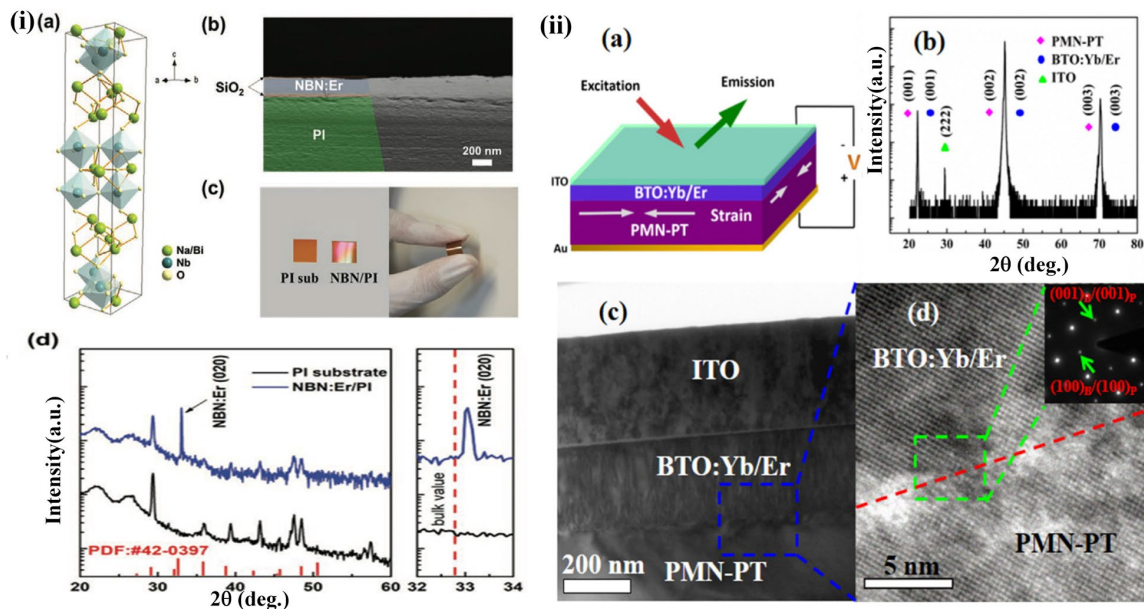


Figure 6. (i) (a) Schematic diagram of NBN unit cell crystal structure. (b) FE-SEM image of cross-section of NBN: Er/PI sample. (c) PI substrate ($1 \times 1 \text{ cm}^2$), optical images of NBN: Er/PI samples in flat and curved states. (d) Left: XRD results of PI substrate and NBN: Er/PI sample, right: narrow range of NBN: Er(020) peak θ - 2θ Spectrum. Reprinted with permission from [44] © 2020 Wiley-VCH. (ii) (a) (BTO: Yb/Er)/PMN-PT upconversion photoluminescence device under external electric field. (b) XRD θ - 2θ Pattern. (c) A low luminance field image. (d) HRTEM image of the interface structure. Insert shows the SAED pattern. Reprinted with permission from [45] © 2014 The Optical Society.

4.4. Sol-Gel Method

Sol-gel is one of the most utilized chemical methods for fabricating thin films. When the sol-gel method is used to prepare thin films, the materials undergo a series of hydrolysis and polycondensation reactions to form colloids in the typical sol-gel process. The sol solution is sprayed, dipped, or spin-coated on the substrate. The residual organic or inorganic compounds are pyrolyzed through the heat treatment process, which finally forms amorphous or crystalline films. Similarly, this can be achieved not only in the preparation of high purity nanoparticle materials and for good uniformity of nanoparticle materials, but also in the preparation of thin films. For example, Yu prepared rare earth Eu-doped $\text{PbZr}_{0.52}\text{Ti}_{0.48}\text{O}_3$ (PZT) thin films by the sol-gel method [48]. They studied the effect of Eu doping on the ferroelectricity of PZT and found that when the concentration of Eu dopant exceeded 1 atom%, the content of the acceptor dopant or B-site substitution increased, which leads to the increase in intrinsic defects and the degradation of ferroelectric behavior of PZT thin films.

4.5. Spray Pyrolysis

In Section 3.3, we introduced the preparation of nanoparticles by spray pyrolysis. The spray pyrolysis solution mainly contains nitrate or chloride. The solution is changed into spray through the ultrasonic atomizer and is guided to the substrate through the carrier gas of humid air. After deposition, the film is usually annealed in various environments, including air, nitrogen, argon, and molding gas. The properties and quality of the film depend on parameters such as spray rate, substrate temperature, ambient atmosphere, and droplet size. In particular, the substrate temperature is the main factor affecting the spray pyrolysis. The advantage of this method is that it does not need a vacuum environment and the cost of preparing large-scale films is low. For instance, Williams used a spray nondecomposition method to obtain Er-doped ZnO thin films [49].

5. Application of Rare-Earth-Doped Ferroelectric Oxides

Rare-earth-doped ferroelectric oxides exhibit superior luminescent and electronic properties and promise great potential for extensive applications. In this section, we introduce several applications of rare-earth-doped ferroelectric oxides, including optical temperature sensing, lighting, and solar cells.

5.1. Optical Temperature Sensing

Optical temperature sensing can be roughly divided into fluorescence intensity optical temperature sensing, fluorescence decay life optical temperature sensing, and fluorescence intensity ratio optical temperature sensing. Fluorescence intensity optical temperature sensing is based on the fluorescence quenching effect. The fluorescence quenching effect is related to temperature. In the luminescence process, the number of phonons involved in the luminescence process in the matrix will increase with the increase of temperature, and the phonons will interact with the electrons in the material, which will produce nonradiative transition and cause the loss of energy. Therefore, with the increase in temperature, the luminous efficiency will decrease, and the luminous intensity will weaken. The optical temperature sensor has the advantages of resistance to electromagnetic interference, wide dynamic range, and reusability. No conversion between electronics and photonics is required at each sensing point, increasing device flexibility and reducing cost. In addition, to be commercially competitive, the matrix structure must be highly stable over a wide range of temperatures and luminescence must be efficient. Fluorescence quenching can be expressed as a formula:

$$\eta = \frac{1}{1 + Ae^{-\frac{\Delta E}{k_B T}}}, \quad (1)$$

η is the luminous efficiency and ΔE is the activation energy. Fluorescence emission intensity is related to fluorescence quantum efficiency. The fluorescence quantum efficiency

is unchanged, and the temperature of the object can be measured by the change of fluorescence intensity. It can be seen from the formula that the monotonically varying fluorescence intensity can represent the temperature change within a certain temperature range. For fluorescence intensity, the fluctuation of the excitation light source power will also affect it. This effect will bring errors to the temperature measurement and affect the test results. The fluorescence decay life-type optical sensing is based on the fluorescence decay life formula:

$$I_t = I_0 e^{-\frac{t}{\tau}}, \quad (2)$$

τ is the fading time constant used to measure the lifetime of the excited state. The fluorescence lifetime is determined by the temperature. When the luminescence is strong enough and the decay rate is not very fast, it is easier to measure the decay lifetime of fluorescence than the spectral measurement. Fluorescence intensity ratio (FIR) optical temperature sensing is based on fluorescence intensity comparison technology. The principle of fluorescence intensity comparison technology is that when the temperature changes, the luminescent center will be affected by temperature and the quench effect, or the energy transfer rate will change the luminescent intensity. The response of different luminescence centers to temperature is not completely consistent, which leads to the change of the fluorescence intensity ratio of the emission peak when two adjacent excited-state energy levels with a thermal coupling relationship in rare-earth ions transition to a low energy level at different temperatures. Therefore, we can measure the temperature by the change of the emission peak ratio corresponding to the thermal coupling energy level. In FIR technology, the fluorescence intensity of the two emission peaks is proportional to the number of particles in the thermal layout at the energy level. The number of particles in the thermal layout satisfies the Boltzmann distribution. The ratio of fluorescence intensity is (this is example one of an equation):

$$FIR = A e^{-\frac{\Delta E}{k_B T}} + B, \quad (3)$$

FIR is the ratio of fluorescence intensity, ΔE is the difference between two thermal coupling energy levels, k is Boltzmann constant, and T is temperature.

From this formula, it can be concluded that the temperature measurement sensitivity S of FIR technology meets:

$$S_R = \frac{dFIR}{dT} = FIR \times \frac{E}{kT^2}, \quad (4)$$

$$S_A = \frac{1}{FIR} \cdot \frac{dFIR}{dT} = \frac{E}{kT^2}, \quad (5)$$

S_R represents the relative sensitivity, which refers to the change of the fluorescence intensity ratio when the temperature changes, and the unit is K^{-1} . S_A represents the absolute brightness, which refers to the percentage of the change value of fluorescence intensity ratio compared with itself when the temperature changes, and the unit $\%K^{-1}$. At present, the optical sensing of rare-earth-doped ferroelectric oxides is mainly studied and applied according to the fluorescence intensity contrast technology.

Zhang reported the study of Er^{3+} doping into ferroelectric material $Bi_3Ti_{0.5}W_{0.5}O$ (BTW) [50]. As shown in Figure 7a, they found that in the temperature range of 83 K~423 K, based on the fluorescence intensity ratio (FIR) of the green emission at 532.6 nm and 549.2 nm, the light temperature sensitivity was found to be $0.00314 K^{-1}$ at 423 K. In addition, Wu et al. reported that Ho^{3+} ions were doped in (K, Na)NbO₃(KNN) ferroelectric materials [51]. By comparing the luminescence intensity and temperature-sensing sensitivity of different Ho^{3+} ($x = 1, 0.5$) doping concentrations (Figure 7b,c), a maximum sensitivity of $0.0075 K^{-1}$ at 430 K was found in the range of 300 K to 650 K by using two green up-conversion FIR techniques from the 5F_4 and 5S_2 levels of Ho^{3+} . Recently, Banwal et al. doped Er^{3+} into $BaBi_2Nb_2O_9$ ferroelectric ceramics [52]. It was found that strong upconversion luminescence is obtained at 549 nm and 527 nm through

$^4S_{3/2} \rightarrow ^4I_{15/2}$, $^2H_{11/2} \rightarrow ^4I_{15/2}$ migration by 980nm laser excitation. FIR is calculated for both green spectra by calculation, and it is found that FIR increases linearly in the temperature range from 300 K to 623 K. This is due to the thermal excitation and quasi-thermal equilibrium process between $^2H_{11/2}$ and $^4S_{3/2}$. FIR technology optimized Er^{3+} -substituted $BaBi_{2-x}Nb_2Er_xO_9$ ceramics at 483 K with a maximum sensitivity of $0.00996 K^{-1}$ ($x = 0.04$) for optical temperature sensing applications with good repeatability and temperature resolution.

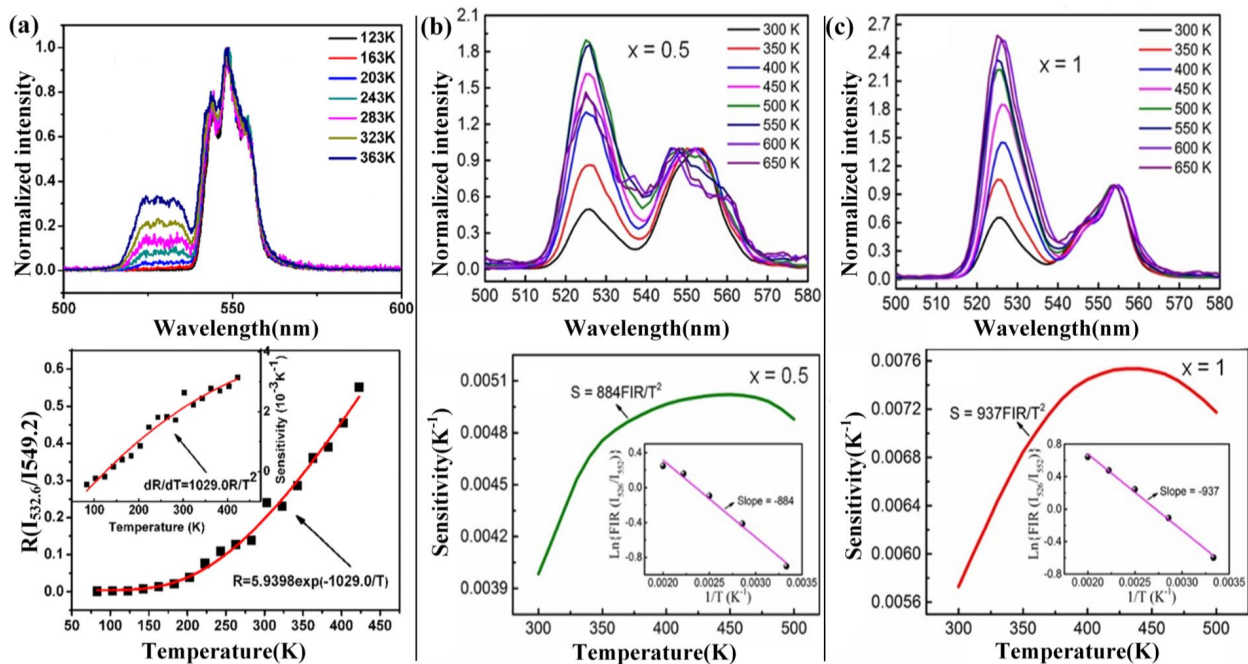


Figure 7. (a) The UC emission spectrum normalized by BTW-0.05 at 123 K, 163 K, 203 K, 243 K, 283 K, and 323 K and the FIR ($R(I_{532.6}/I_{549.2})$) emitted by green UC at 83 K~423 K are shown as a function of absolute temperature. The inset shows the temperature dependence of sensitivity. Reprinted with permission from [50] © 2017 AIP. (b,c) is the sensitive pair of the UC green emission of KNNLB-Ho- x ($x = 0.5, 1$) sample in the range of 300 K–500 K and the temperature sensor of KNNLB-Ho- x , in which the inset shows the log normal diagram of fir and reverse absolute temperature. Reprinted with permission from [51] © 2018 American Ceramic Society.

5.2. Lighting

Rare-earth ions' luminescent materials have many applications in the field of solid-state lighting because of their special properties. LED (light emitting diode) is the most representative light source of solid-state lighting at present. Compared with the traditional lighting source, it has the advantages of small size, strong planarization designability, long life, energy saving, environmental protection, and no pollution, which make it the most potential green lighting source in the 21st century.

There are three solutions to realize the white LED for lighting:

- White light is synthesized by blue LED and $(Y_{1-a}Gd_a)_3(Al_{1-b}Ga_b)_5O_{12}: Ce^{3+}$ (YAG) phosphor.
- Red light (400 nm) or ultraviolet LED (360 nm, etc.) excites red, green, and blue phosphors to synthesize white light.
- Semiconductor chips emitting red, green, and blue light are used for combined luminescence.
- Titanate ferroelectrics, such as $BaTiO_3$ (BTO) with perovskite ABO_3 structure, are studied by doping rare-earth ions. As can be seen from Figure 8a, Zhang synthesized Yb^{3+} , Er^{3+} , and Tm^{3+} tri-doped BTO phosphors with different doping concentrations by the solid-phase reaction method [20]. By precisely controlling the dopant concentration, the color of UC emission can be adjusted. They achieved the best white luminescence

with color coordinates ($x = 0.328$, $y = 0.352$) by adjusting the relative RGB intensity (BTO:5%Yb³⁺, 0.02%Er³⁺, 0.2%Tm³⁺).

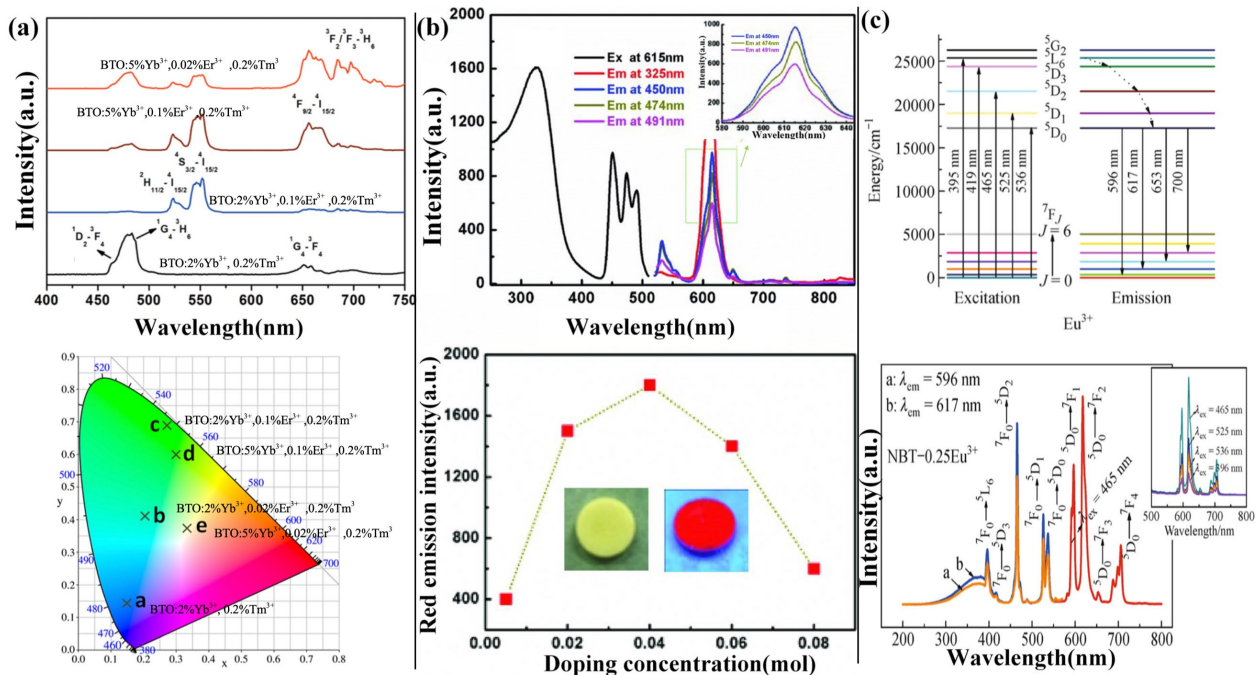


Figure 8. (a) UC emission spectra of BTO:Ln³⁺ phosphors under 980 nm laser excitation and CIE chromaticity diagrams for BTO:Ln³⁺ phosphors under 980 nm laser excitation. Reprinted with permission from [20] © 2013 AIP. (b) The room temperature emission (Em) and excitation (Ex) spectra of doped Pr show that the intensity is 0.04 and show the relationship between emission intensity and Pr concentration (the left inset shows the prepared target without excitation, and the right inset shows the case of excitation with a commercial ultraviolet lamp at 365 nm). Reprinted with permission from [53] © 2013 Taylor & Francis. (c) The possible transition relatives to excitation and emission processes of Eu³⁺ ions and the PL spectra of NBT-0.25Eu³⁺ sample excited by different wavelengths ($\lambda_{\text{ex}} = 396$ nm, 465 nm, 525 nm and 536 nm). Reprinted with permission from [54] © 2016 Springer.

In addition, there are other ferroelectrics, such as bismuth layer ferroelectrics. The crystal structure of BLSFs consists of pseudoperovskite layers, which interleave bismuth oxide (Bi₂O₂)²⁺ layers along the c-axis. CaBi₂Nb₂O₉(CBNO) is a member of BLSFs with $m = 2$ and a high Curie temperature of ~ 930 °C.

Peng et al. doped Pr³⁺ into the ferroelectric material CBNO. They found that an excitation band located between 430 nm and 500 nm appeared under the excitation of a 365 nm laser (Figure 8b) [53]. This excitation band is a transition from the ground state ³H₄ of Pr³⁺ to the excited state ³P_J ($J = 0, 1, 2$) via a typical f-f transition. This excited state covers all commercial blue light emitting diodes (LED), so CBNO doped with Pr³⁺ can be applied to white LEDs based on blue light LEDs. Jiang et al. also found the strongest excitation peak of 465 nm in Eu³⁺-doped Na_{0.5}Bi_{4.5}Ti₄O₁₅-based(NBT) ferroelectrics, which matched well with the output wavelength of commercial GaN-based blue LEDs, indicating the potential application of Eu³⁺-doped NBT in W-LEDs (Figure 8c) [54].

5.3. Solar Cell

Rare-earth-doped photoconversion materials have been widely concerned by researchers because they can effectively improve the photoelectric conversion efficiency of solar cells. At present, silicon solar cells are ideal and commonly used silicon solar cells. The problem of silicon solar cells is that the light of each band of solar energy is not fully utilized, resulting in a lowered conversion efficiency. The main solar spectrum modulation schemes by optical conversion materials include upconversion and downconversion

luminescent materials and wavelength conversion materials. Light-emitting materials convert several infrared photons in the solar spectrum that cannot be absorbed by solar cells into visible or near-infrared light that can be used by batteries through upconversion materials. The main feature of this process is that several photons are converted into one photon. Luminescent material converts the light in the solar spectrum whose energy is twice or higher than the peak energy absorbed by the battery into photons that can be absorbed by the two batteries through downconversion material. Down-shift material converts a high-energy photon into photons that can be absorbed by a battery. For some single-phase ferroelectric oxide materials, they have the characteristics of a direct band gap semiconductor, good chemical stability, high electron mobility, and are used in solar cell applications.

Different applications focus on different aspects. For optical temperature sensing, temperature sensitivity is the most important performance marker. This process is mainly based on the relationship between temperature and luminous efficiency. Different ferroelectric oxide materials have different responses to temperature. So, it is very important to find suitable ferroelectric oxide materials for doping. Solar cells are different. Solar cells focus on the conversion efficiency of solar energy. With the doping of rare-earth ions, the structure of doped ferroelectric oxides changes, leading to the improvement of the performance of solar cells. For the mechanism of the perovskite solar cells, when the perovskite absorption layer absorbs sunlight, it is excited to generate electron hole pairs (carriers), then the carriers are separated, electrons are injected into the electron transport material layer (anode), holes are injected into the hole transport material layer (cathode), and finally the circuit current is formed by recycling on the metal pair electrode through the external circuit. The working principle behind photodetectors is based on the internal photoelectric effect. The working mechanism of photodetectors, in which the optical signal is converted into the electrical signal, includes the following four steps: (1) the generation of excitons from photon absorption, (2) the diffusion of the generated excitons to the interface between the donor and acceptor to produce charge transfer excitons, (3) the separation of charge transfer excitons into free charges at the donor/acceptor interface, and (4) the collection of free charges at the electrodes [55]. In principle, solar cells are similar to photodetectors. However, the solar cell mainly depends on the energy collection efficiency, and the photodetector mainly depends on the response to the light signal. In addition, the fundamental principles of solid-state dye-sensitized solar cells are similar to those of liquid electrolyte-based dye-sensitized solar cells except for electron hopping through the hole transporting material (HTM) layer [56].

Lotey et al. synthesized undoped and Gd-doped BiFeO₃ nanoparticles by the sol-gel method successfully, which were applied to the preparation of dye-sensitized solar cells (DSSC) [32]. Gd was doped in BiFeO₃, which improves the energy conversion efficiency of DSSC. They found that the doping of Gd has a significant effect on the photocurrent or photocurrent density, which will increase with the increase in Gd doping concentration. The 12% Gd-doped BiFeO₃ achieved a high energy conversion efficiency of 3.85%, which is more than 100% higher than the undoped BiFeO₃. Goel et al. synthesized pure ZnO nanorods and lanthanum-doped ZnO nanorods using a co-precipitation method and prepared dye-sensitized solar cells (DSSCs) using ZnO and La-doped ZnO nanorods [57]. They found that the conversion efficiency and short-circuit current density of La-doped ZnO nanorod-based DSSCs were higher than that of pure ZnO, with a conversion efficiency of 0.36% and a short-circuit current density of 1.31 mA/cm². The XRD and DSSC applications of the synthesized ZnO nanorod are shown in Figure 9.

5.4. Other Applications

In addition, some studies have explored some new applications of rare-earth-doped ferroelectric oxides. For instance, Zhao uses NBN-doped Er³⁺ to make devices on a LiNbO₃(LN) substrate, which can emit visible surface acoustic waves (SAW) through lanthanide elements [58]. They developed a SAW in situ detection technology for light emission of lanthanide-doped ferroelectrics. This technique is based on the regular change

of the luminous intensity of the time-integrated PL spectrum of NBN: Er films under the action of different power surface acoustic waves. As shown in Figure 10d, the greater the power of SAW, the weaker the luminous intensity. High-power SAWs result in the decrease of PL intensity of the films, which is attributed to the lattice distortion caused by the propagation of acoustic waves. The frequency dependence of PL modulation is a good indicator of SAW-driven resonant oscillation. This research promotes the integration of SAW and lanthanide luminescence. From the basic research of lanthanide materials to the development of novel SAW-based devices, it will bring broad application prospects. Device structure, film quality analysis, and spectral analysis are shown in Figure 10.

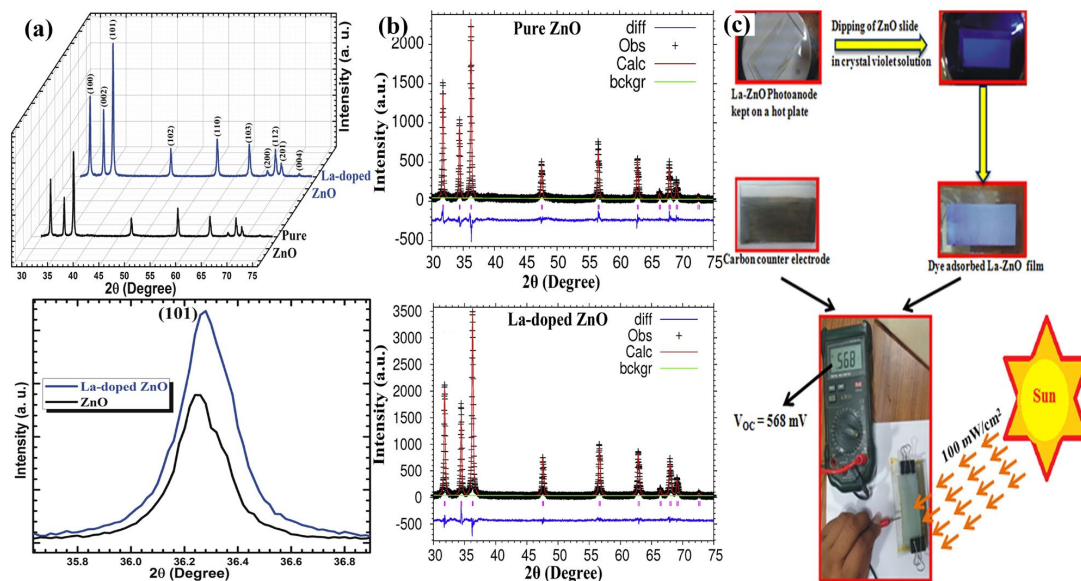


Figure 9. (a) and (b) are the XRD of pure ZnO and La-ZnO. (c) The application of DSSC. Reprinted with permission from [57] © 2017 Elsevier Ltd.

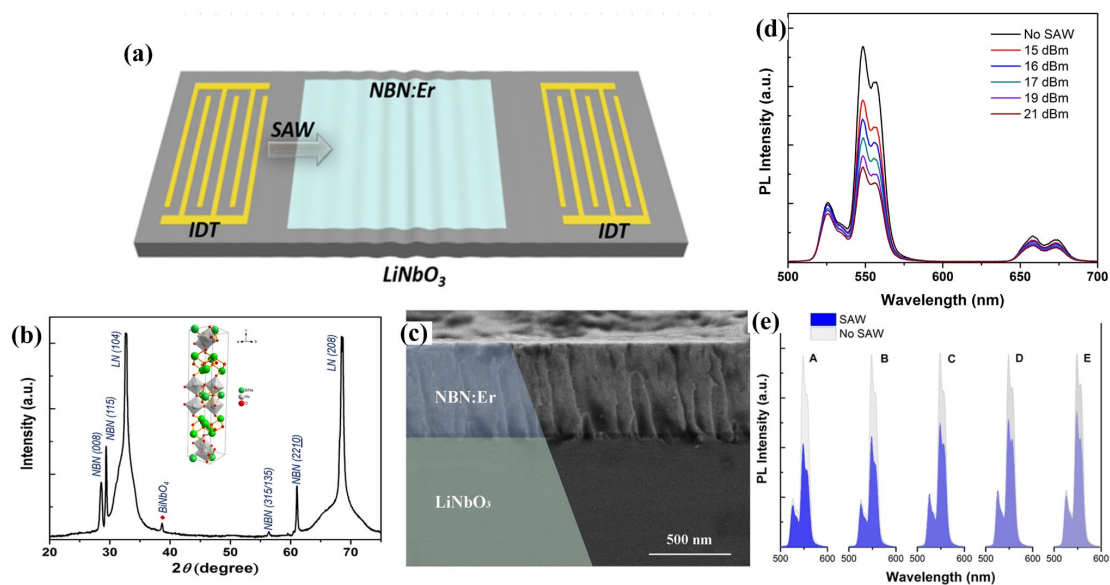


Figure 10. (a) Device structure diagram. (b) XRD of NBN: Er/LN. (c) FE-SEM image of cross-section of NBN: Er/LN sample. (d) Time-integrated PL spectra of the NBN: Er film with and without SAW of different powers under 980 nm laser excitation. (e) PL spectra of five points along the acoustic pathway with and without SAW modulation. Reprinted with permission from [58] 2020 Wiley-VCH.

6. Summary and Outlook

This article mainly introduces the preparation of rare-earth-doped ferroelectric materials and their related applications. Rare-earth-doped ferroelectric materials are capable of emitting luminescence covering the UV to NIR region, through upconversion or downconversion processes. Common physical and chemical methods used for fabricating rare-earth-doped ferroelectric oxides and thin films are introduced. Rare-earth-doped ferroelectric oxides have found widespread applications. The luminescence properties of rare-earth ions are affected by temperature, which leads to fluorescence quenching or energy transfer efficiency reduction. Rare-earth-doped ferroelectric oxides have been used for optical temperature sensing, which is mainly realized by FIR technology. In terms of lighting, white light emission is realized by controlling the concentration of doped ions and adjusting the emission color through three or more doped rare-earth ions. The light emission center of rare-earth ions can cover the excitation wavelength of current commercial LEDs, which finally realize LED light emission. The upconversion and downconversion solar cell converts the solar spectrum, which is suitable for the performance improvement of various solar cells. For different applications, some material properties cannot be met, such as the poor high-temperature resistance of some oxides. Nonradiative multiphoton relaxation is an important manner that impairs the luminescent performance. High phonon energies of ferroelectric oxides would weaken the luminescence properties of some rare earth ion-doped ferroelectric oxides and will lead to the phenomenon of weak luminescence. The coupling between piezoelectricity, ferroelectricity, and optoelectronic properties in rare-earth-doped ferroelectric oxides provides more freedom to design novel photonic devices. However, the coupling efficiency is still relatively low. The brittle nature of conventional ferroelectric oxides impedes the development of flexible optoelectronics. These problems need to be solved. Some rare earth ion-doped ferroelectric oxides will lead to the phenomenon of weak luminescence. These are all problems that need to be solved. Moreover, the applications of rare earth ion-doped ferroelectric oxides are mostly in the laboratory stage, which is far from actual commercial use. They also need to compete with the existing ones on the market.

For future development and applications, the brightness and efficiency of rare-earth-doped ferroelectric oxides should be further improved. The composition and fabrication conditions can be optimized. The interaction between doped rare-earth ions and ferroelectric hosts also has great influence on the luminescent properties of as-grown samples. Recent studies have shown that physical fields such as the electric field, strain, and temperature can modulate the luminescent properties in situ, which could help to reveal the mechanism and improve the luminescent efficiency. Moreover, significant effort has been devoted to realize optical control of ferroelectric polarization, which can offer more freedom to develop ferroelectric-based devices [59]. As for applications, thin film structures are more suitable to be integrated with various substrates, which provide a platform for multifunctional optoelectronic devices. It is important to develop rare-earth-doped ferroelectric thin films integrated with flexible substrates, which are suitable for developing flexible optoelectronics.

Author Contributions: Writing—original draft preparation, T.B. and T.Z.; writing—review and editing, Y.Z.; funding acquisition, Y.Z.; All authors have read and agreed to the published version of the manuscript.

Funding: This research was funded by the National Natural Science Foundation of China (No. 11874230, 12274243, 52233014) and the Fundamental Research Funds for the Central Universities.

Data Availability Statement: Not applicable.

Conflicts of Interest: The authors declare no conflict of interest.

References

1. Zhang, Y.; Hao, J. Metal-ion doped luminescent thin films for optoelectronic applications. *J. Mater. Chem. C* **2013**, *1*, 5607–5618. [[CrossRef](#)]
2. Peng, D.; Zou, H.; Xu, C.; Wang, X.; Yao, X. Er doped BaBi₄Ti₄O₁₅ multifunctional ferroelectrics: Up-conversion photoluminescence, dielectric and ferroelectric properties. *J. Alloys Compd.* **2013**, *552*, 463–468. [[CrossRef](#)]
3. Liu, Y.; Tu, D.; Zhu, H.; Chen, X. Lanthanide-doped luminescent nanoprobe: Controlled synthesis, optical spectroscopy, and bioapplications. *Chem. Soc. Rev.* **2013**, *42*, 6924–6958. [[CrossRef](#)] [[PubMed](#)]
4. Chen, H.; Dong, Z.; Zhao, Y.; Li, S.; Du, X.; Wu, Z.; Liu, W.; Zhang, Y. In-situ tailoring upconversion processes from lanthanide ions doped ferroelectric films through piezoelectric strain. *J. Lumin.* **2020**, *219*, 116914. [[CrossRef](#)]
5. Peng, D.; Wang, X.; Xu, C.; Yao, X.; Lin, J.; Sun, T. Bright upconversion emission, increased T_c, enhanced ferroelectric and piezoelectric properties in Er-doped CaBi₄Ti₄O₁₅ multifunctional ferroelectric oxides. *J. Am. Ceram. Soc.* **2013**, *96*, 184–190. [[CrossRef](#)]
6. Wang, Y.; Zheng, K.; Song, S.; Fan, D.; Zhang, H.; Liu, X. Remote manipulation of upconversion luminescence. *Chem. Soc. Rev.* **2018**, *47*, 6473–6485. [[CrossRef](#)]
7. Tomar, A.; Singh, M.; Singh, S.; Sharma, L.; Arya, S.; Kasana, S. Ultraviolet Quantum Cutting through down Conversion Luminescence Behaviour of Er³⁺ Substituted Sr_{0.7}Bi_{2.2}Nb₂O₉ (BLFS) Ceramics. *Integr. Ferroelectr.* **2020**, *204*, 33–37. [[CrossRef](#)]
8. Sun, L.; Qiu, Y.; Liu, T.; Peng, H.; Deng, W.; Wang, Z.; Shi, L. Visible-light sensitized sol-gel-based lanthanide complexes (Sm, Yb, Nd, Er, Pr, Ho, Tm): Microstructure, photoluminescence study, and thermostability. *RSC Adv.* **2013**, *3*, 26367–26375. [[CrossRef](#)]
9. Wang, D.; Li, S.; Chan, H.W.; Choy, C. Optical and electro-optic anisotropy of epitaxial Ba_{0.7}Sr_{0.3}TiO₃ thin films. *Appl. Phys. Lett.* **2010**, *96*, 061905. [[CrossRef](#)]
10. Chang, Q.; Zhou, X.; Zhou, X.; Chen, L.; Xiang, G.; Jiang, S.; Li, L.; Li, Y.; Tang, X. Strategy for optical thermometry based on temperature-dependent charge transfer to the Eu³⁺ 4f-4f excitation intensity ratio in Sr₃Lu_{(VO₄)₃:Eu³⁺ and CaWO₄:Nd³⁺. *Opt. Lett.* **2020**, *45*, 3637–3640. [[CrossRef](#)]}
11. Zhang, Y.; Hao, J.; Mak, C.L.; Wei, X. Effects of site substitutions and concentration on upconversion luminescence of Er³⁺-doped perovskite titanate. *Opt. Express* **2011**, *19*, 1824–1829. [[CrossRef](#)]
12. Zhang, Y.; Jie, W.; Chen, P.; Liu, W.; Hao, J. Ferroelectric and piezoelectric effects on the optical process in advanced materials and devices. *Adv. Mater.* **2018**, *30*, 1707007. [[CrossRef](#)]
13. Sun, H.; Peng, D.; Wang, X.; Tang, M.; Zhang, Q.; Yao, X. *Strong Red Emission in Pr Doped (Bi_{0.5}Na_{0.5})TiO₃ Ferroelectric Ceramics*; American Institute of Physics: College Park, MD, USA, 2011.
14. Wei, T.; Zhao, C.; Zhou, Q.; Li, Z.; Wang, Y.; Zhang, L. Bright green upconversion emission and enhanced ferroelectric polarization in Sr_{1-1.5x}Er_xBi₂Nb₂O₉. *Opt. Mater.* **2014**, *36*, 1209–1212. [[CrossRef](#)]
15. Cui, R.-R.; Deng, C.-Y.; Gong, X.-Y.; Li, X.-C.; Zhou, J.-P. Luminescence properties of Eu³⁺ doped CaBi₂Ta₂O₉ bismuth layered-structure ferroelectrics. *Mater. Res. Bull.* **2013**, *48*, 4301–4306. [[CrossRef](#)]
16. Wei, X.K.; Bihlmayer, G.; Zhou, X.; Feng, W.; Kolen'ko, Y.V.; Xiong, D.; Liu, L.; Blügel, S.; Dunin-Borkowski, R.E. Discovery of Real-Space Topological Ferroelectricity in Metallic Transition Metal Phosphides. *Adv. Mater.* **2020**, *32*, 2003479. [[CrossRef](#)]
17. Wei, X.K.; Domingo, N.; Sun, Y.; Balke, N.; Dunin-Borkowski, R.E.; Mayer, J. Progress on Emerging Ferroelectric Materials for Energy Harvesting, Storage and Conversion. *Adv. Energy Mater.* **2022**, *2022*, 2201199. [[CrossRef](#)]
18. Puggioni, D.; Rondinelli, J.M. Designing a robustly metallic noncentrosymmetric ruthenate oxide with large thermopower anisotropy. *Nat. Commun.* **2014**, *5*, 1–9. [[CrossRef](#)]
19. Sun, H.L.; Wu, X.; Chung, T.H.; Kwok, K.W. In-situ electric field-induced modulation of photoluminescence in Pr-doped Ba_{0.85}Ca_{0.15}Ti_{0.90}Zr_{0.10}O₃ lead-free ceramics. *Sci. Rep.* **2016**, *6*, 1–8. [[CrossRef](#)]
20. Zhang, Y.; Hao, J. Color-tunable upconversion luminescence of Yb³⁺, Er³⁺, and Tm³⁺ tri-doped ferroelectric BaTiO₃ materials. *J. Appl. Phys.* **2013**, *113*, 184112. [[CrossRef](#)]
21. Wang, Z.; Li, W.; Chu, R.; Hao, J.; Xu, Z.; Li, G. Strong luminescence and high piezoelectric properties in Pr-doped (Ba_{0.99}Ca_{0.01})(Ti_{0.98}Zr_{0.02})O₃ multifunctional ceramics. *J. Alloys Compd.* **2016**, *689*, 30–35. [[CrossRef](#)]
22. Yao, Y.; Liu, W.; Chan, Y.; Leung, C.; Mak, C. Studies of rare-earth-doped BiFeO₃ ceramics. *Int. J. Appl. Ceram. Technol.* **2011**, *8*, 1246–1253. [[CrossRef](#)]
23. Zhou, S.; Lin, D.; Su, Y.; Zhang, L.; Liu, W. Enhanced dielectric, ferroelectric, and optical properties in rare earth elements doped PMN-PT thin films. *J. Adv. Ceram.* **2021**, *10*, 98–107. [[CrossRef](#)]
24. Verma, V. Structural, electrical and magnetic properties of rare-earth and transition element co-doped bismuth ferrites. *J. Alloys Compd.* **2015**, *641*, 205–209. [[CrossRef](#)]
25. Waindich, A.; Möbius, A.; Müller, M. Corrosion of Ba_{1-x}Sr_xCo_{1-y}FeyO_{3-δ} and La_{0.3}Ba_{0.7}Co_{0.2}Fe_{0.8}O_{3-δ} materials for oxygen separating membranes under Oxycoal conditions. *J. Membr. Sci.* **2009**, *337*, 182–187. [[CrossRef](#)]
26. Nagai, T.; Ito, W.; Sakon, T. Relationship between cation substitution and stability of perovskite structure in SrCoO_{3-δ}-based mixed conductors. *Solid State Ion.* **2007**, *177*, 3433–3444. [[CrossRef](#)]
27. Abdullah, N.A.; Hasan, S.; Osman, N. Role of CA-EDTA on the synthesizing process of cerate-zirconate ceramics electrolyte. *J. Chem.* **2013**, *2013*, 908340. [[CrossRef](#)]

28. Lichtenberg, F.; Herrnberger, A.; Wiedenmann, K. Synthesis, structural, magnetic and transport properties of layered perovskite-related titanates, niobates and tantalates of the type $A_nB_nO_{3n+2}$, $A'A_{k-1}B_kO_{3k+1}$ and $A_mB_{m-1}O_{3m}$. *Prog. Solid State Chem.* **2008**, *36*, 253–387. [[CrossRef](#)]
29. Cushing, B.L.; Kolesnichenko, V.L.; O'Connor, C.J. Recent advances in the liquid-phase syntheses of inorganic nanoparticles. *Chem. Rev.* **2004**, *104*, 3893–3946. [[CrossRef](#)]
30. Goh, G.K.; Haile, S.M.; Levi, C.G.; Lange, F.F. Hydrothermal synthesis of perovskite and pyrochlore powders of potassium tantalate. *J. Mater. Res.* **2002**, *17*, 3168–3176. [[CrossRef](#)]
31. Sardar, K.; Lees, M.R.; Kashtiban, R.J.; Sloan, J.; Walton, R.I. Direct hydrothermal synthesis and physical properties of rare-earth and yttrium orthochromite perovskites. *Chem. Mater.* **2011**, *23*, 48–56. [[CrossRef](#)]
32. Mostafa, M.; Alrowaili, Z.; Rashwan, G.; Gerges, M. Ferroelectric behavior and spectroscopic properties of La-Modified lead titanate nanoparticles prepared by a sol-gel method. *Heliyon* **2020**, *6*, e03389. [[CrossRef](#)]
33. Lotey, G.S.; Verma, N. Gd-doped BiFeO₃ nanoparticles—A novel material for highly efficient dye-sensitized solar cells. *Chem. Phys. Lett.* **2013**, *574*, 71–77. [[CrossRef](#)]
34. Rajbhar, M.K.; Ashina, A.; Ramasamy, E.; Mallick, S.; Rao, T.N.; Veerappan, G. A facile co-precipitation method for synthesis of Zn doped BaSnO₃ nanoparticles for photovoltaic application. *Mater. Chem. Phys.* **2021**, *258*, 123939.
35. Wang, Y.; Cai, F.; Guo, P.; Lei, Y.; Xi, Q.; Wang, F. Short-Time Hydrothermal Synthesis of CuBi₂O₄ Nanocolumn Arrays for Efficient Visible-Light Photocatalysis. *Nanomaterials* **2019**, *9*, 1257. [[CrossRef](#)]
36. Chen, G.; Wang, W. Role of freeze drying in nanotechnology. *Dry. Technol.* **2007**, *25*, 29–35. [[CrossRef](#)]
37. Klvana, D.; Vaillancourt, J.; Kirchnerova, J.; Chaouki, J. Combustion of methane over La_{0.66}Sr_{0.34}Ni_{0.3}Co_{0.7}O₃ and La_{0.4}Sr_{0.6}Fe_{0.4}Co_{0.6}O₃ prepared by freeze-drying. *Appl. Catal. A Gen.* **1994**, *109*, 181–193. [[CrossRef](#)]
38. Ghaffarian, H.R.; Saiedi, M.; Sayyadnejad, M.A.; Rashidi, A.M. Synthesis of ZnO Nanoparticles by Spray Pyrolysis Method. *Iran. J. Chem. Chem. Eng.* **2011**, *30*, 1–6.
39. Zhang, M.; Wang, J.; Xia, Y.; Liu, Z. Microwave synthesis of spherical spinel LiNi_{0.5}Mn_{1.5}O₄ as cathode material for lithium-ion batteries. *J. Alloys Compd.* **2012**, *518*, 68–73. [[CrossRef](#)]
40. De Bonis, A.; Teghil, R. Ultra-short pulsed laser deposition of oxides, borides and carbides of transition elements. *Coatings* **2020**, *10*, 501. [[CrossRef](#)]
41. Beke, S. A review of the growth of V₂O₅ films from 1885 to 2010. *Thin Solid Film.* **2011**, *519*, 1761–1771. [[CrossRef](#)]
42. Dong, F.; Chen, H.; Dong, Z.; Du, X.; Chen, W.; Qi, M.; Shen, J.; Yang, Y.; Zhou, T.; Wu, Z. Mechanically induced enhancement and modulation of upconversion photoluminescence by bending lanthanide-doped perovskite oxides. *Opt. Lett.* **2022**, *47*, 706–709. [[CrossRef](#)] [[PubMed](#)]
43. Chen, W.; Dong, Z.; Chen, H.; Shen, J.; Du, X.; Dong, F.; Zhou, T.; Huang, W.; Wu, Z.; Liu, W. Control of upconversion luminescence by tailoring energy migration in doped perovskite superlattices. *Opt. Lett.* **2022**, *47*, 1250–1253. [[CrossRef](#)] [[PubMed](#)]
44. Chen, H.; Dong, Z.; Chen, W.; Sun, L.; Du, X.; Zhao, Y.; Chen, P.; Wu, Z.; Liu, W.; Zhang, Y. Flexible and Rewritable Non-Volatile Photomemory Based on Inorganic Lanthanide-Doped Photochromic Thin Films. *Adv. Opt. Mater.* **2020**, *8*, 1902125. [[CrossRef](#)]
45. Wu, Z.; Zhang, Y.; Bai, G.; Tang, W.; Gao, J.; Hao, J. Effect of biaxial strain induced by piezoelectric PMN-PT on the upconversion photoluminescence of BaTiO₃: Yb/Er thin films. *Opt. Express* **2014**, *22*, 29014–29019. [[CrossRef](#)] [[PubMed](#)]
46. Song, T.; Bachelet, R.; Saint-Girons, G.; Solanas, R.; Fina, I.; Sánchez, F. Epitaxial ferroelectric La-doped Hf_{0.5}Zr_{0.5}O₂ thin films. *ACS Appl. Electron. Mater.* **2020**, *2*, 3221–3232. [[CrossRef](#)]
47. Safi, I. Recent aspects concerning DC reactive magnetron sputtering of thin films: A review. *Surf. Coat. Technol.* **2000**, *127*, 203–218. [[CrossRef](#)]
48. Yu, Y.; Chan, H.; Wang, F.; Zhao, L. Effects of rare earth Eu doping on ferroelectric properties of PbZr_{0.52}Ti_{0.48}O₃ thin films by sol-gel methods. *Microelectron. Eng.* **2003**, *66*, 726–732. [[CrossRef](#)]
49. Williams, T.; Hunter, D.; Pradhan, A.; Kityk, I. Photoinduced piezo-optical effect in Er doped ZnO films. *Appl. Phys. Lett.* **2006**, *89*, 043116. [[CrossRef](#)]
50. Zhang, Y.; Li, J.; Chai, X.; Wang, X.; Li, Y.; Yao, X. Enhanced electrical properties, color-tunable up-conversion luminescence, and temperature sensing behaviour in Er-doped Bi₃Ti_{1.5}W_{0.5}O₉ multifunctional ferroelectric ceramics. *J. Appl. Phys.* **2017**, *121*, 124102. [[CrossRef](#)]
51. Wu, X.; Lin, J.; Chen, P.; Liu, C.; Lin, M.; Lin, C.; Luo, L.; Zheng, X. Ho³⁺-doped (K, Na)NbO₃-based multifunctional transparent ceramics with superior optical temperature sensing performance. *J. Am. Ceram. Soc.* **2019**, *102*, 1249–1258. [[CrossRef](#)]
52. Banwal, A.; Bokolia, R. Enhanced upconversion luminescence and optical temperature sensing performance in Er³⁺ doped BaBi₂Nb₂O₉ ferroelectric ceramic. *Ceram. Int.* **2022**, *48*, 2230–2240. [[CrossRef](#)]
53. Peng, D.; Zou, H.; Xu, C.-N.; Li, J.; Wang, X.; Yao, X. Photoluminescent and dielectric characterizations of Pr doped CaBi₂Nb₂O₉ multifunctional ferroelectrics. *Ferroelectrics* **2013**, *450*, 113–120. [[CrossRef](#)]
54. Jiang, X.-a.; Jiang, X.-p.; Chen, C.; Tu, N.; Chen, Y.-j.; Zhang, B.-c. Photoluminescence and electrical properties of Eu³⁺-doped Na_{0.5}Bi_{4.5}Ti₄O₁₅-based ferroelectrics under blue light excitation. *Front. Mater. Sci.* **2016**, *10*, 31–37. [[CrossRef](#)]
55. Yang, D.; Ma, D. Development of organic semiconductor photodetectors: From mechanism to applications. *Adv. Opt. Mater.* **2019**, *7*, 1800522. [[CrossRef](#)]
56. Park, N.-G. Perovskite solar cells: An emerging photovoltaic technology. *Mater. Today* **2015**, *18*, 65–72. [[CrossRef](#)]

57. Goel, S.; Sinha, N.; Yadav, H.; Joseph, A.J.; Kumar, B. Experimental investigation on the structural, dielectric, ferroelectric and piezoelectric properties of La doped ZnO nanoparticles and their application in dye-sensitized solar cells. *Phys. E Low Dimens. Syst. Nanostructures* **2017**, *91*, 72–81. [[CrossRef](#)]
58. Zhao, Y.; Yuan, Y.; Chen, H.; Chen, W.; Du, X.; Gong, C.; Lin, L.; Luo, W.; Liu, W.; Zhang, Y. In Situ Probing of Surface Acoustic Waves by Interfacing with Lanthanide Emitters. *Adv. Opt. Mater.* **2021**, *9*, 2001760. [[CrossRef](#)]
59. Guo, J.; Chen, W.; Chen, H.; Zhao, Y.; Dong, F.; Liu, W.; Zhang, Y. Recent progress in optical control of ferroelectric polarization. *Adv. Opt. Mater.* **2021**, *9*, 2002146. [[CrossRef](#)]